Research Article Vol. 28, No. 11 / 25 May 2020 / Optics Express 16673
Optics EXPRESS

Polarimetric imaging in backscattering for the structural characterization of strongly scattering birefringent fibrous media

ARUSHI JAIN,[1] ANJANI K. MAURYA,[2,3,4] LEONIE ULRICH,[1] MICHAEL JAEGER,[1] RENÉ M. ROSSI,[4] ANTONIA NEELS,[2] PHILIPPE SCHUCHT,[5] ALEX DOMMANN,[2,3] MARTIN FRENZ,[1,*] AND H. GÜNHAN AKARÇAY[1]

[1]*Biomedical Photonics Department , Institute of Applied Physics, University of Bern, Sidlerstrasse 5 CH-3012 Bern, Switzerland*
[2]*Empa, Swiss Federal Laboratories for Materials Science and Technology, Center for X-ray Analytics, Lerchenfeldstrasse 5 CH-9014 St.Gallen, Switzerland*
[3]*Cellular and Biomedical Sciences, Faculty of Medicine, University of Bern, Mittelstrasse 43 CH-3012 Bern, Switzerland*
[4]*Empa, Swiss Federal Laboratories for Materials Science and Technology, Laboratory for Biomimetic Membranes and Textiles, Lerchenfeldstrasse 5 CH-9014 St.Gallen, Switzerland*
[5]*Department of Neurosurgery, University hospital Bern, Freiburgstrasse 16 CH - 3010 Bern, Switzerland*
[*]*martin.frenz@iap.unibe.ch*

Abstract: Interpreting the polarimetric data from fiber-like macromolecules constitutive of tissue can be difficult due to strong scattering. In this study, we probed the superficial layers of fibrous tissue models (membranes consisting of nanofibers) displaying varying degrees of alignment. To better understand the manifestation of membranes' degree of alignment in polarimetry, we analyzed the spatial variations of the backscattered light's Stokes vectors as a function of the orientation of the probing beam's linear polarization. The degree of linear polarization reflects the uniaxially birefringent behavior of the membranes. The rotational (a-)symmetry of the backscattered light's degree of linear polarization provides a measure of the membranes' degree of alignment.

1. Introduction

Polarimetric examination of tissues has been of great interest over the past decades [1–5]. Biological tissues contain elongated fiber-like macromolecules (including collagen fibers in skin and in tendons, muscle fibers, keratin, myofibrils in skeletal muscles, axons in white matter, *etc.*), and those fibers are organized in such a way that they exhibit a certain degree of structural anisotropy and anisotropy in dielectric response [6,7]. These effects are often coupled [8] and manifest themselves via birefringence [9], which can be observed by using polarized light [6].

Experimental observations have shown that the retardance and depolarization induced by birefringent tissues can be used as indicators to assess their microstructure (in tendon [10], in skeletal and cardiac muscle [11,12], or in skin [13–18]) and thus, be helpful for diagnostics (*e.g.*, for cancer, cirrhosis, and different types of fibrosis) and for the studying of mechanical properties of connective tissues [19]. Moreover, it has been reported that the birefringence/retardance effects exhibited by aligned fibrous tissue are extremely sensitive to small pathological alterations: Tissue containing highly aligned anisotropic molecules, such as linear collagen and myocytes, exhibit higher birefringence (*eg.* certain types of skin scars [20]) than structures with weaker anisotropy (*e.g.* cancer [3] or scar tissue in the myocardium [21,22]).

#390303 https://doi.org/10.1364/OE.390303
Journal © 2020 Received 19 Feb 2020; revised 11 May 2020; accepted 11 May 2020; published 19 May 2020

Optics EXPRESS

These promising findings have reinvigorated the need to gain further insights into the underlying physics of polarized light propagation in fibrous media and, thereby, better understand the correlations between tissues' polarimetric properties and their fibrous microstructure, in particular their *degree of alignment* [23–26]. The entirety of the polarimetric properties of any tissue is encoded in its Perrin-Mueller (PM) matrix [27]. However, extracting information on the microstructure of tissues by deciphering their PM matrix remains a challenging endeavor [11,28–35], because "the physical meaning of the [PM] matrix elements is often unclear, especially for the anisotropic scattering materials" [36]. This is primarily due to the fact that polarimetric properties such as retardance and depolarization are intertwined, which is not readily apparent in the PM matrix [37]. This is even more true when the polarimetric measurements are performed in the backscattering geometry (which is of greater interest for medical applications) than in transmission.

A number of researchers are working on the interpretation of the PM matrix elements by applying mathematical factorization/decomposition techniques: A comprehensive overview on this topic is given in [7,38,39]. However, because tissues are not pure retarders or polarizers/diattenuators, employing such decomposition methods does not necessarily solve the issue of understanding their polarimetric behavior; rather, in most cases, it merely shifts it to the interpretation of the extracted quantities. Nonetheless, some of these decomposition methods have become popular on the application end of polarimetry. For example, the polar decomposition, introduced by Lu and Chipman [40], is widespread in the realm of tissue optics to generate high contrast images that could be valuable for diagnostics (*e.g.*, [12,22,41–45]). This polar decomposition is based on the assumption that the probed system is a non-commutative [46,47] chain of optical components (diattenuator, retarder and depolarizer), which does not necessarily do justice to the complexity of the system. Novel decomposition techniques are being developed [30,48–52] and allow for the generation of alignment maps in tissue and fibrous materials, but fully understanding the underlying physics remains a difficult undertaking.

Three other prevalent branches of research try to circumvent the problem by proposing analysis methods that do not rely on PM matrix decomposition techniques. The first one focusses on extracting relevant metrics from the PM matrix, without resorting to a decomposition, based on empirical observations [36,53–57]. Yet, as stated by the Authors, "to find out more quantitative and precise relations between the PM matrix parameters and microstructural properties of tissues, statistical studies on different tissue samples are still needed" [56]. Statistical analysis methods are at the heart of the second branch of research [58–61] and constitute an encouraging prospect for the better understanding of the interactions between polarized light and tissue. The third and last research branch is arguably simpler and provides a more direct understanding of the polarized light scattering by observing how tissue like materials' polarimetric response changes with the probing light's polarization state [37,62–68].

The techniques mentioned above, be it with or without decomposition of the PM matrix, have enabled important advances in terms of detecting and measuring birefringence, determining the orientation of well-aligned fibrous structures, and generating contrast images that discriminate different types of tissue. Here, we pursued these efforts with an experimental study that was aimed at better understanding how the degree of alignment of tissue-like, fibrous materials can be assessed from polarimetric images obtained in the backscattering geometry. For this purpose, we focused on a system where, following the measurement and analysis procedures introduced in [37] (and in line with the last aforementioned studies), we illuminate the membranes with a focussed beam and analyse the spatial variations of the backscattered light's Stokes vectors as a function of the probing beam's polarization. To investigate the relation between the degree of alignment and polarimetric parameters, we probed electrospun Poly(vinylidene fluoride-cohexafluoropropylene) (PVDFhfp) membranes composed of nanofibers. We restricted our investigation to a well-defined scenario where these nanofiber's degree of alignment was varied in a controlled fashion, and where

Optics EXPRESS

they were majoritarily aligned along planes quasi-parallel to the imaging plane of the polarimeter. In this paper, we introduce a methodology that helps establish correlations between the structural anisotropy in the membranes and the birefringence they exhibit (whereby birefringence refers to the combined effect of intrinsic and form birefringence). We further show how this correlation could be used to deduce the degree of alignment of the nanofibers constitutive of the membrane.

2. Materials and methods

2.1. Probed samples: electrospun PVDFhfp membranes with varying degree of alignment

The membranes consisting of nanofibers in this study were produced by electrospinning technique, using a custom-built device: the production and characterization of these membranes are thoroughly described in [69]. In brief, pellets of PVDFhfp of molecular weight of $\sim 400000\,\mathrm{g.mol^{-1}}$ were dissolved in a concentration of 35 % w/v in dimethylfomamide (DMF). Afterwards, the dissolved solution was filled in a 3 ml syringe connected with a 21 G blunt metallic needle. A high voltage of +14 kV at the needle and −5 kV at the collector was set. The flow rate of $20\,\mu\mathrm{l.min^{-1}}$ was set by using a microfluidics pump. Nanofibers were collected on aluminium foils by either using a flat plate or a standard rotating drum collector of diameter of 5 cm at a distance of 25 cm from needle to the surface of the collectors. The electrospinning allowed to produce membranes where the nanofibers are aligned majoritarily along parallel planes. The flat plate was used to generate *non-aligned* membranes, where the orientation of the nanofibers is quasi-random, whereas the rotating drum collector was used to produce membranes with nanofibers that are majoritarily aligned along the same direction (in the remainder of this paper, we refer to this direction as the nanofibers' *mean alignment direction*). Producing membranes with different degrees of alignment of the nanofibers was made possible by operating the rotating drum at different speeds. It was demonstrated, by performing a spatial correlation analysis on scanning electron microscope (SEM) micrographs and Small Angle X-ray scattering (SAXS), that increasing the rotation speed of the collector drum also increased the degree of alignment in the membranes, *i.e.*, reduced the misalignment between the nanofibers [69]. The SEM micrographs were also used to evaluate the average nanofiber diameter in all membranes. An average diameter of 490 ± 230 nm was measured for non-aligned as well as aligned samples, which is within the range of fiber diameters encountered in biological tissue [70–75].

Here, we probed one non-aligned membrane and four membranes with aligned nanofibers, collected with 1000, 1500, 2000 and 2100 rotations per minute (rpm) of the drum. A photograph and SEM image of such a membrane are shown in Fig. 1. The degree of alignment in the membranes collected at 1000, 1500, and 2000 was quantified in [69]: whereas there is clear reduction in the misalignment of the nanofibers when increasing the rotation speed from 1000 to 2000 rpm, the misalignment does not change significantly between 1000 and 1500 rpm. Furthermore, on the photograph in Fig. 1, it can be seen, that these membranes are opaque, strongly scattering. We also observed that their thickness is non-uniform across the membrane. Thus, we performed our polarimetric measurements on areas ($\sim 4\,\mathrm{mm^2}$) where the thickness was comparable from one membrane to another. The thickness of the membranes was measured using a microscope (Olympus Vanox). The holder onto which the membranes were fixed (without the aluminium collector foil) was mounted on a micrometer stage. The holder was positioned twice: first to focus the microscope on the holder surface (adjacent to the fixed membrane) and second to focus the microscope on a point on the membrane surface. The difference between the two positions yielded an estimation for the membrane thickness at the measurement point. The thicknesses of the areas we probed are given in Table 1. These estimates were obtained by repeating the aforementioned procedure three times with 12 random points across the chosen area.

Optics EXPRESS

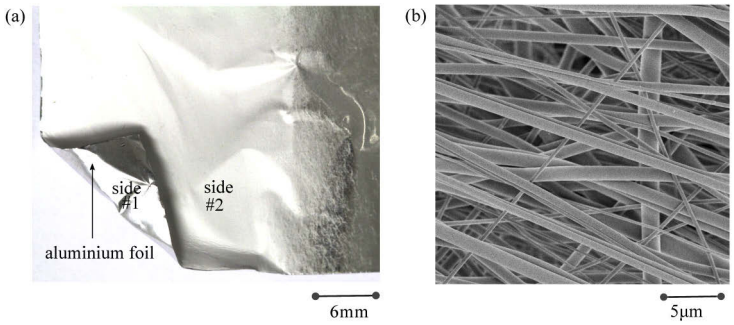

Fig. 1. **(a)**: Photograph of the PVDFhfp membrane collected on an aluminium foil (side #1 facing the aluminium foil) at 2100 rpm, where the uneven thickness is visible. **(b)**: Scanning electron microscope micrograph (recorded on side #2 with a Hitachi-High s-4800 microscope) of the same membrane where the aligned nanofibers are revealed.

Table 1. Thicknesses of the membranes at the probed regions.

PVDFhfp membranes	Non-aligned	1000 rpm	1500 rpm	2000 rpm	2100 rpm
Estimated thickness (mm)	0.335±0.039	0.192±0.033	0.178±0.006	0.107±0.0098	0.158±0.018

2.2. Polarimetric microscope

The imaging polarimeter we used to probe the electrospun membranes is the one described in [37]: see the sketch in Fig. 2. To avoid ambiguities, we have drawn in this figure all the coordinate systems (chosen to be right handed) involved in our measurements. The polarimetric instrument has two arms that are perpendicular to each other. The illumination arm includes the polarization state generator (PSG), and the detection arm comprises a standard two-lens system and polarization state analyzer (PSA). A tunable super continuum laser (SoleaR by PicoQuant, adjustable wavelength from 480 nm to 900 nm, coupled into a single mode fiber) is used as the light source. After emission from the single mode fiber, the laser beam is collimated using a lens (LC). The beam is directed through the PSG, and guided towards the surface of the probed membrane by a non-polarizing beam-splitter cube (50:50, maintaining polarization to 0.5% at $\pi/4$ incidence). With the PSG, composed of a linear polarizer (LP, Nanoparticle Linear Polarizer, Thorlabs, extinction ratio 1:100'000) and two liquid crystal variable retarders (LCR, Meadowlark optics, controlled via computer), any arbitrary polarization state can be generated. For the first retarder, the fast axis is aligned at $\pi/4$ with respect to the $x-$ and $y-$axes of the lab frame, while for the second retarder, the fast-axis is aligned with the $y-$axes of the lab frame. The polarized illumination beam is focussed onto the probed membrane's surface by an objective lens (L2) of focal length $f = 30$ mm. To determine the $1/e^2$ spot radius (43 μm), the sample was replaced with a camera (customized Pixelink for beam profiling) and a Gaussian profile was fitted to the intensity distributions imaged for different z-positions. The backscattered light propagates through the two-lens system consisting of an objective lens L2 and a second lens L1 (focal length $f = 60$ mm). The numerical aperture of the imaging system (in this study 0.133) is determined by an iris located in the back focal plane of L2. The illumination beam is slightly tilted (~ 0.14 rad) to avoid recording specular reflection. The PSA located between L2 and L1 is composed of the same elements as the ones in the PSG, but positioned in reverse order. To image the backscattered light (with a magnification of ~ 1.9), a CCD chip (ptGray grasshopper, 16bit, 2448×2048 pixels) was placed at the end of the detection arm. All measurements presented

Optics EXPRESS

in this work were performed at λ =785 nm (so as to remain within the *diagnostic window* that is favorable for tissue diagnostics). The coherence length can be flexibly chosen by the laser system control, and was set to approximately 150 μm. The magnification and wavelength values were chosen empirically and kept the same for all membranes. Moreover, the membranes were attached to a computerized scanning stage (H101P2BX ProScan stage operated via a V31XYZE controller, both from PRIOR Scientific) to scan the sample in the $x, y-$direction.

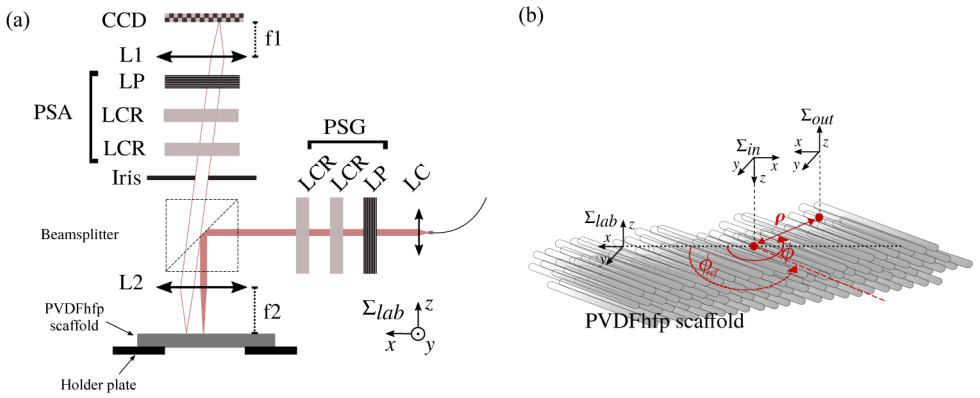

Fig. 2. **(a)**: Schematic drawing (not to scale) of the polarimetric imaging setup used to probe the electrospun membranes in the backscattering geometry. This instrument has two arms: an illumination and a detection arm containing polarization state generator (PSG) and the polarization state analyzer (PSA), respectively. LC, L1, and L2 denote the lenses. LCR are liquid crystal retarders and LP are linear polarizers. The membranes were probed at λ = 785 nm with a focussed beam. The backscattered intensity distribution is recorded by a CCD chip positioned at the end of the detection arm. Σ_{lab} denotes the laboratory frame. **(b)**: Schematic representation of all the right-handed coordinate systems involved in the experiment and the positioning of the membranes. The laboratory frame Σ_{lab} corresponds to the one sketched on the left image. Σ_{in} is the input frame in which the illumination beam's polarization state is defined. The detection frame Σ_{out} attached to the CCD camera coincides with Σ_{lab}. For the radial analysis carried out in this paper, each point on the probed membrane's surface is defined by the polar coordinates (ρ, ϕ). For the measurements, the membranes were roughly positioned such that nanofibers were aligned on average along $\phi_{ref} \approx 3\pi/4$ and the probing beam was focussed at $\mathbf{r}(\rho = 0, \phi = 0)$. The nanofibers sketched here represent an ideal case, with *perfect alignment*.

As explained in [37], the polarimetric instrument was calibrated with the eigenvalue calibration method (ECM) [76] in its *extended* version [77] and validated by comparing measurements on colloidal suspensions with Monte Carlo simulations.

2.3. Measurement procedure

In order to probe the different membranes with the polarimetric microscope, we mounted each membrane on a holder plate having a circular window (diameter 1 cm) at its center, so that the non-collector side of the membrane (side #2 in Fig. 1) faced the window. The purpose of this window was to record exclusively the light backscattered from the membranes, without having to worry about possible reflections at the membrane-holder interface (as sketched in Fig. 2(a)). The mounted membranes were placed in a freezer for approximately 10 mins, which subsequently allowed the easy removal of the aluminum foil on which the membranes were collected, thereby exposing their collector side (side #1 in Fig. 1(a)) towards to objective lens (L2) and this, without altering the membranes. Note that the measurements were performed in air, *i.e.* with a high refractive index contrast between fibers and surrounding medium.

Optics EXPRESS

The mean alignment direction of the nanofibers in the membranes collected on the rotating drum was distinguishable under the microscope: see background images in Fig. 3 recorded by illuminating the membranes' surface with widefield illumination, using an external white light source. This allowed positioning the membranes' side #1 under the polarimetric microscope by approximately aligning the nanofibers at a reference azimuthal angle $\phi_{ref} = 3\pi/4$ (the non-aligned membrane was positioned randomly) in the x, y-plane, *i.e.*, the imaging plane. Note that even though the surface images were valuable for the approximate estimation of the nanofiber's mean alignment direction, they can be deceiving with respect to the nanofibers' degree of alignment. For sake of reproducibility, each membrane was probed at four different points $\mathbf{r}_{i=1\cdots4}$ on the chosen areas.

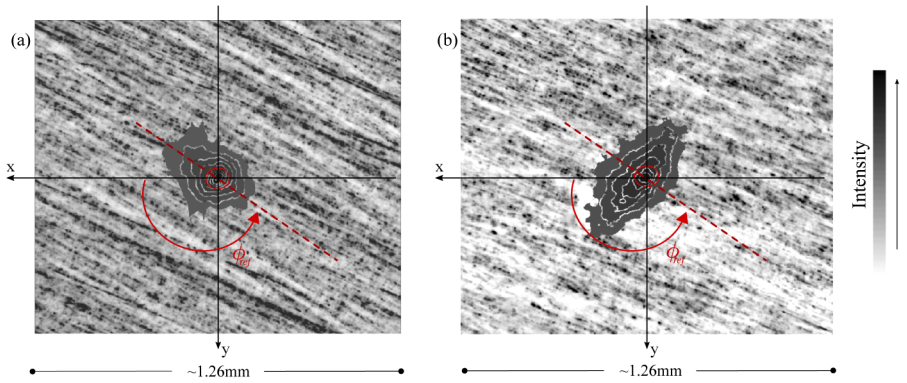

Fig. 3. Intensity distributions (grey shaded, filled iso-contours) of the light backscattered from the membrane collected at 2100 rpm, superimposed on the image of the membrane's surface, separately recorded with widefield, white light illumination. **(a)**: side #2; **(b)**: collector side #1 (recall Fig. 1). The images are shown in the frame Σ_{out}. The red circles at the center of the images represent the focal spot size and position of the probing beam, which was here linearly polarized ($+\pi/4$ in Σ_{in}). As depicted in Fig. 2, the nanofibers were approximately aligned (with the help of the widefield surface images) at an azimuthal angle $\phi_{ref} = 3\pi/4$.

The distinction between both sides #1 and #2 is relevant in that they display differences in terms of the degree of alignment: On the collector side #1 of the membranes, the variability of fiber orientation was constrained to a plane (observed as surface flatness), and thus the degree of alignment was determined by the rotation speed in the most well defined way. On side #2, however, the membranes were relatively rough. We illustrate the contrast between both sides with the examples in Fig. 3. We probed both surfaces of the membrane collected at 2100 rpm with linearly polarized light and recorded the intensity distributions of the backscattered light (see the filled iso-countours). On side #1, the elliptical distribution stretched along the direction perpendicular to the nanofibers' mean alignment direction reflects a distinct alignment, whereas side #2 is inconclusive. For a consistent comparison of degree of alignment, we therefore chose to probe the membranes only on their side #1 [78,79].

The polarimeter was used to probe each point with the focussed laser beam and to sequentially record images of the intensity distribution of the backscattered light for different pairs of illumination (PSG) and detection (PSA) states. The spatial PM matrix $\mathbf{M}(\rho, \phi)$ was then calculated according to the procedure outlined in [37]. Noise reduction was achieved by taking the average of 200 images for each intensity measurement, and in addition the background noise/dark-current of the CCD was subtracted.

Optics EXPRESS

2.4. Representation and analysis of the polarimetric measurements

As already mentioned in the introduction and explained more in detail in [37], instead of directly inspecting the measured PM matrix $\mathbf{M}(\rho, \phi)$, we take a step back and adopt a more rudimentary approach. Namely, we take a closer look at the spatial variations of the backscattered light's polarization across the membranes' surfaces, separately for different polarization states of the probing beam. The polarization ellipse of the backscattered light at a point (ρ, ϕ) on a membrane's surface is mathematically described by a Stokes vector $\vec{S}_{out}(\rho, \phi) = (I_{out}(\rho, \phi), Q_{out}(\rho, \phi), U_{out}(\rho, \phi), V_{out}(\rho, \phi))^T$. $\vec{S}_{out}(\rho, \phi)$ can be calculated in a straightforward fashion for any input state $\vec{S}_{in}$ by a simple matrix multiplication: $\vec{S}_{out}(\rho, \phi) = \mathbf{M}(\rho, \phi)\vec{S}_{in}$ (recall that $\vec{S}_{in}$ is expressed in Σ_{in} and $\vec{S}_{out}$ in Σ_{out}).

For a more intuitive and intelligible appreciation of the spatial variations of the polarization ellipses, we plot and analyze the *polarization ellipse parameters* (PEPs) introduced in [37] individually: *orientation*, *ellipticity*, *helicity*, and *degree of polarization*. In addition to these PEPs, we examine here the degree of linear polarization, which can be a valuable indicator, together with the ellipticity, to assess the birefringence induced by the anisotropic nanofibers. These PEPs are independent of the choice of Σ_{in} and Σ_{out}, making the interpretation easier. They can be calculated from the Stokes vector elements [25]:

- **Degree of polarization** As stated by Al Qasimi et al., "The degree of polarization of a quasi-monochromatic light beam at a point ρ, ϕ is the ratio of the (averaged) intensity of the polarized portion of the beam to its total (averaged) intensity, both taken at that point" [80]. Following this definition, we can express the degree of polarization Π of the light backscattered at a point (ρ, ϕ) as:

$$\Pi(\rho, \phi) = \frac{\sqrt{(Q_{out}^2(\rho, \phi) + U_{out}^2(\rho, \phi) + V_{out}^2(\rho, \phi))}}{I_{out}(\rho, \phi)}. \tag{1}$$

- **Degree of linear polarization** Similarly, the degree of linear polarization Π_L of the backscattered light is given by:

$$\Pi_L(\rho, \phi) = \frac{\sqrt{(Q_{out}^2(\rho, \phi) + U_{out}^2(\rho, \phi))}}{I_{out}(\rho, \phi)}. \tag{2}$$

- **Ellipticity and helicity** The ellipticity $\epsilon(\rho, \phi)$ of the polarization state of the backscattered light at a point (ρ, ϕ) can be quantified as [81]:

$$\epsilon(\rho, \phi) = \frac{M_{min}(\rho, \phi)}{M_{max}(\rho, \phi)} \tag{3}$$

where $M_{min}(\rho, \phi)$ denotes to the semi-minor, $M_{max}(\rho, \phi)$ to the semi-major axis of the polarization ellipse. $\epsilon(\rho, \phi) = 1$ refers to circular polarization and $\epsilon(\rho, \phi) = 0$ to perfectly linear polarization. The semi-minor and semi-major axes can be determined as:

$$\begin{aligned} M_{max}^2(\rho, \phi) = &\frac{1}{2}\sqrt{Q_{out}^2(\rho, \phi) + U_{out}^2(\rho, \phi) + V_{out}^2(\rho, \phi)} \\ &+ \frac{1}{2}\sqrt{Q_{out}^2(\rho, \phi) + U_{out}^2(\rho, \phi)} \end{aligned} \tag{4}$$

$$\begin{aligned} M_{min}^2(\rho, \phi) = &\frac{1}{2}\sqrt{Q_{out}^2(\rho, \phi) + U_{out}^2(\rho, \phi) + V_{out}^2(\rho, \phi)} \\ &- \frac{1}{2}\sqrt{Q_{out}^2(\rho, \phi) + U_{out}^2(\rho, \phi)}. \end{aligned} \tag{5}$$

As for the helicity, it is merely:

$$h(\rho, \phi) = \mathrm{sgn}(V_{out}(\rho, \phi)). \tag{6}$$

Optics EXPRESS

- **Orientation** Finally, the orientation angle ψ of the polarization ellipse of the light backscattered at a point (ρ, ϕ) is given by [81]:

$$\tan\left[2\psi(\rho,\phi)\right] = \frac{U_{out}(\rho,\phi)}{Q_{out}(\rho,\phi)} \text{ with } -\pi/2 \leq \psi(\rho,\phi) \leq \pi/2. \tag{7}$$

Analogously to the study carried out in [37], we relate, in the following, the spatial variations of these PEPs to the microstructure of the probed membranes.

3. Results and discussion

3.1. Manifestation of anisotropy and birefringence in the PEPs

We begin our investigation by identifying the polarimetric parameters that differ between the non-aligned membrane, where the nanofiber orientation is random, and the membrane collected at 2100 rpm, whose nanofibers display a high degree of alignment [69]. Figure 4 show the PEPs-images recorded at a single point $\mathbf{r}_{i=1}$ from the non-aligned membrane (a) and the membrane collected at 2100 rpm (b) for three pairs of orthogonal polarization states of the probing beam (columns): $\left\{(\vec{S}_{LX}, \vec{S}_{LY}), (\vec{S}_{L+}, \vec{S}_{L-}), (\vec{S}_{C+}, \vec{S}_{C-})\right\}$ (see [37,82,83]). Differences between the two sets of PEPs are apparent at first glance. The differences between the intensity distributions already highlight the rather isotropic behavior of the non-aligned membrane and the anisotropic nature of the membrane collected at 2100 rpm. Confirming the results shown in Fig. 3, the intensity distributions of the light backscattered from the latter membrane are elliptical (Fig. 4(b)), stretched along the azimuthal profile perpendicular to the nanofiber alignment direction [53,78,84]. This, irrespective of the probing beam's polarization state $\vec{S}_{in}$. The same does not hold true for the intensity distributions recorded from the non-aligned membrane (Fig. 4(a)). This non-aligned membrane is *rotationally symmetric*, *i.e.*, rotating the linear input state $\vec{S}_{in}$ is equivalent to rotating the recorded image. This can be seen in the other PEPs-images: $\Pi(\rho, \phi)$- and $\Pi_L(\rho, \phi)$-images (second and third rows, respectively), as well as in the helicity-weighted ellipticity images (fourth row) and the orientation of the polarization ellipses $\psi(\rho, \phi)$-images (fifth row). All in all, the PEPs recorded from the non-aligned membrane are reminiscent of those recorded from polystyrene spheres diluted in water [37]. It is interesting to notice that, when randomly oriented, the asymmetric/anisotropic nanofibers' polarimetric response resembles that of perfectly symmetric/isotropic spheres. As an additional note, we would like to underline the fact that the retardance measured in backscattering from the non-aligned membrane when probed with linearly polarized light (see the non-null ellipticity in Fig. 4(a)) is not an indication of birefringence. The same observation has been made in [37] for perfectly isotropic colloidal suspensions of polystyrene spheres (with a large size parameter), where the retardance could be explained by the scattering geometry.

The PEPs recorded from the membrane collected at 2100 rpm display very different characteristics. Firstly, no rotational symmetry is visible. Secondly, the elliptical, stretched patterns visible in the intensity distributions are accentuated in the $\Pi(\rho, \phi)$- and $\Pi_L(\rho, \phi)$-images: The backscattered light is strongly polarized along the azimuthal profiles that are perpendicular to the nanofiber alignment direction, irrespectively of $\vec{S}_{in}$ (linear or circular). This further reveals the anisotropic nature of the membrane. The relation between the anisotropy and the birefringence induced can be found by comparing the $\Pi(\rho, \phi)$- and $\Pi_L(\rho, \phi)$-images. Whereas the $\Pi(\rho, \phi)$-images seem to be relatively independent of $\vec{S}_{in}$, the $\Pi_L(\rho, \phi)$-images demonstrate that the backscattered light preserves the linear polarization of the probing beam significantly more (darker purple patterns in Fig. 4(b)) when $\vec{S}_{in} = \vec{S}_{L+}$ and $\vec{S}_{in} = \vec{S}_{L-}$, *i.e.*, the polarization is approximately parallel or perpendicular to the nanofiber alignment direction, than when the polarization is along other directions ($\vec{S}_{in} = \vec{S}_{LX}$ and $\vec{S}_{in} = \vec{S}_{LY}$, in which case the backscattered light is mostly elliptically polarized). These results are comparable to the ones yielded by the

Optics EXPRESS

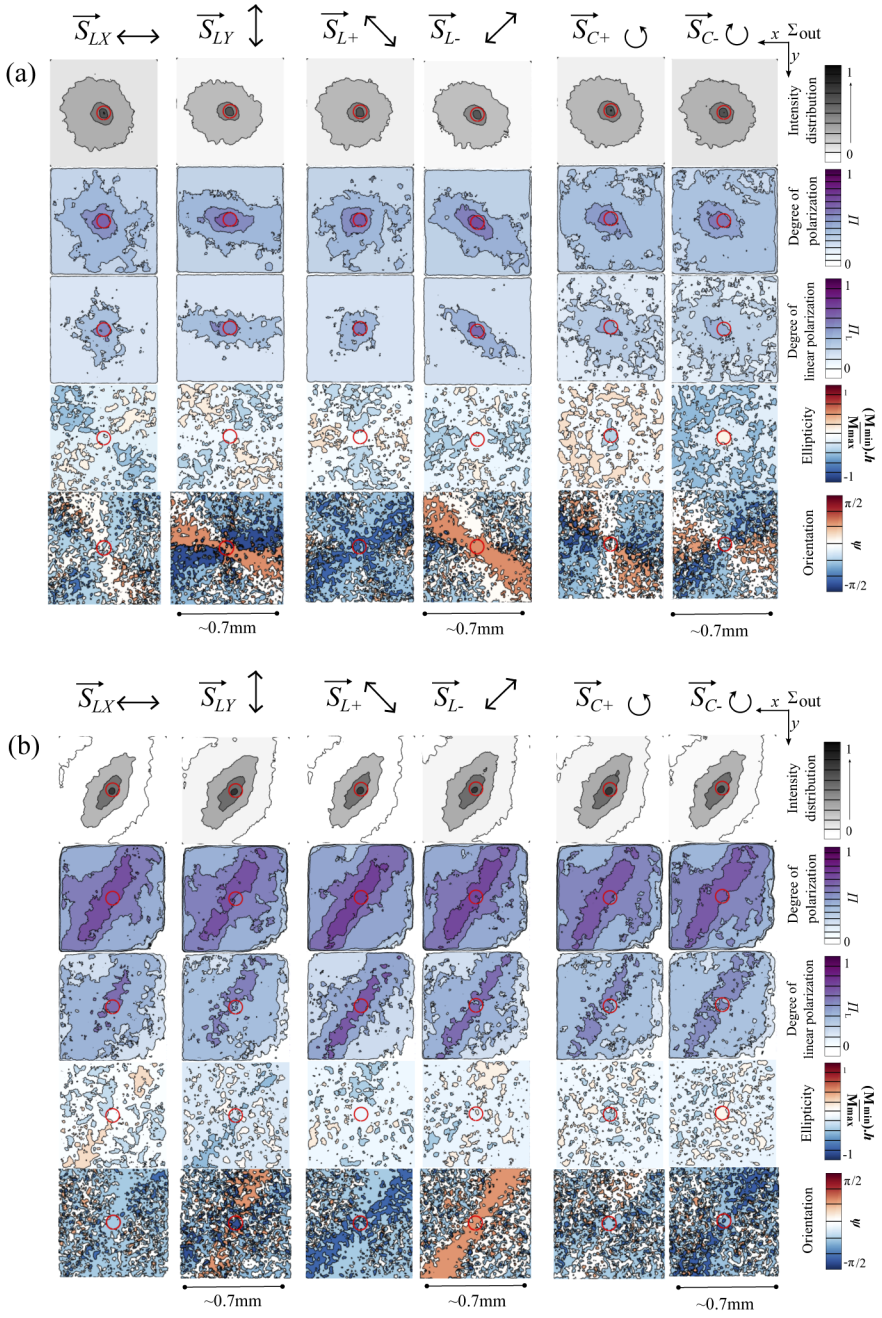

Fig. 4. Measured polarization ellipse parameters (PEPS) for **(a)** the non-aligned membrane and **(b)** the membrane aligned at 2100 rpm for three pairs of orthogonal states of the probing beam (*columns*): $\left\{(\vec{S}_{LX}, \vec{S}_{LY}), (\vec{S}_{L+}, \vec{S}_{L-}), (\vec{S}_{C+}, \vec{S}_{C-})\right\}$. The different PEPs-images are shown with filled iso-contours to make them more interpretable. Note that the contour levels are fixed among panels corresponding to the same parameter, and the color hues show the average pixel value between the corresponding levels. First row: intensity distribution, second row: degree of polarization; third row: degree of linear polarization; fourth row: helicity-weighted ellipticity; fifth row: orientation. The red circle at the center of the images represents the probing beam's focal spot size and position.

Optics EXPRESS

experiments using cellophane tape in [37] and by the simulations reported in [85] and indicate that this strongly aligned, anisotropic membrane mimics the behavior of a uniaxially birefringent material, where the mean alignment direction of the nanofibers defines the optic axis. Looking at the $\psi(\rho, \phi)$-images in the PEPs, it can also be seen that not only the linearity, but also the orientation of the probing beam's polarization is preserved.

According to the picture of a uniaxally birefringent material, one would expect to see, in addition to the preservation of the linear states along the optic axis, the retardance that appears in other directions. This retardance would be visible in the degree of circular polarization (as reported in [85] or [68]), *i.e.*, in the ellipticity images. Yet, even though this retardance is partially visible, there is no pattern in the ellipticity images that can be as clearly identified as in the $\Pi_L(\rho, \phi)$-images This is attributable to the fact that the retardance/ellipticity measured here is not only induced by the birefringence of the membrane, but also by the scattering geometry, as stated above. Consequently, since the degree of linear polarization of the backscattered light seems to be a more reliable indicator of the membranes' birefringence, we investigate, in the following, the relation between the $\Pi_L(\rho, \phi)$-images and the membranes' degree of alignment.

3.2. *Correlations between the* $\Pi_L(\rho, \phi)$*-images and the membranes' degree of alignment*

We show, in Fig. 5, the $\Pi_L(\rho, \phi)$-images recorded from the four aligned membranes (collected at **(a)**: 1000 rpm; **(b)**: 1500 rpm ; **(c)**: 2000 rpm; **(d)**: 2100 rpm). Recall from Sec. 2.1 that the higher the rotation speed at which the membranes have been collected, the higher the degree of alignment. The polarization of the probing beam $\vec{S}_{in} = \vec{S}_{L+}$ was kept parallel to the approximate nanofiber alignment direction. To showcase the reproducibility of our results, the measurements are shown at different points $\mathbf{r}_{i=1\cdots4}$ on the surface of the membranes and similarly to Fig. 3, the $\Pi_L(\rho, \phi)$-images are superimposed on the image of the membrane's surface, recorded separately with widefield illumination. This combined image reveals that increasing the degree of alignment increases the structural anisotropy (again, in agreement with the results shown in [78,79]) and thereby the birefringent properties of the membranes. Indeed, it can be seen from the measurements at $\mathbf{r}_{i=1\cdots4}$ that the higher the degree of alignment, the more the elliptical patterns in the $\Pi_L(\rho, \phi)$-images are stretched in the direction perpendicular to the mean nanofiber alignment direction and the stronger is the preservation of the degree of linear polarization. This suggests that, with increasing degree of alignment, the membranes behave more and more like a uniaxial birefringent material where the mean nanofiber alignment direction determines the optic axis. (Note once more that the surface images can be misleading, *i.e.*, that the different nanofiber alignments visible to the eye do not necessarily reflect the differences in their degree of alignment).

Various publications in the biomedical field have reported that highly aligned, anisotropic molecules, such as linear collagen and myocytes, exhibit higher birefringence than structures with weaker anisotropy, such as cancerous or scar tissue (*e.g.*, [12,21]). As such, and as already acknowledged in the introduction, there is a great medical interest in identifying a quantitative indicator that would allow to derive, from the anisotropy and birefringence exhibited by fibrous tissues, their degree of alignment.

Here, we investigate the possibility of doing so by analyzing the patterns in the $\Pi_L(\rho, \phi)$-images and quantifying their dependence on the probing beam's polarization state $\vec{S}_{in}$. Hence, we performed a radial analysis of the $\Pi_L(\rho, \phi)$-images to determine, for a given polarization state of the probing beam $\vec{S}_{in}$, both the azimuthal direction, ϕ_{max}, in which the elliptical patterns in the $\Pi_L(\rho, \phi)$-images are stretched, and how strongly the linear polarization of the probing beam is preserved along ϕ_{max}. For each membrane and at each measurement point $\mathbf{r}_{i=1\cdots4}$, we calculate the mean degree of linear polarization $\langle \Pi_L(\phi) \rangle_\rho$, along lines that pass through the center of the probing beam (origin of the polar coordinate frame) with different azimuthal angles ϕ. The total

Optics EXPRESS

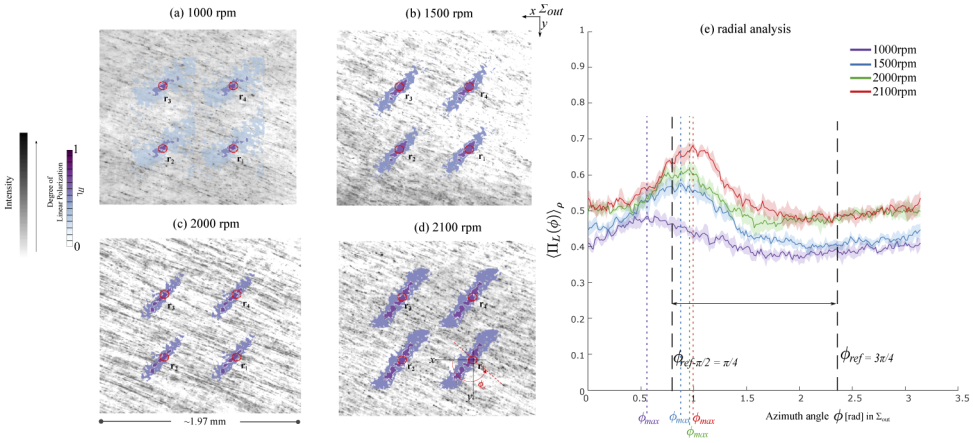

Fig. 5. **(a)-(d)** Degree of linear polarization $\Pi_L(\rho, \phi)$-images of the light backscattered from four different points $\mathbf{r}_{i=1\cdots4}$ on the surface of the four aligned membranes (collected at **(a)**: 1000 rpm; **(b)**: 1500 rpm ; **(c)**: 2000 rpm; **(d)**: 2100 rpm). These $\Pi_L(\rho, \phi)$-images are superimposed on the image of the membrane's surface, separately recorded with widefield, white light illumination (similarly to Fig. 3). The red circles at the center of the images represent the focal spot size and position of the probing beam, which was here linearly polarized ($\vec{S}_{in} = \vec{S}_{L+}$ in Σ_{in}), approximately parallel to the nanofiber alignment direction. In order to quantify the differences between the $\Pi_L(\rho, \phi)$-images, we performed, around each $\mathbf{r}_i$, a *radial analysis*, by calculating, for different azimuthal angles ϕ, the mean degree of linear polarization $\langle \Pi_L(\phi) \rangle_\rho$ along the radial profile at ϕ. Results are shown in **(e)**: each curve corresponds to a different membrane, where the solid line is $\langle \Pi_L(\phi) \rangle_\rho$ averaged over $\mathbf{r}_{i=1\cdots4}$, and the shaded area the standard deviation between those points. The positions of the peaks denote the azimuthal direction ϕ_{max} of the stretch. It can be seen that the patterns are not exactly stretched in the direction perpendicular to the approximate alignment direction ϕ_{ref} of the nanofibers.

averaging length covers $\pm 300\,\mu m$ from the coordinate origin. See Fig. 5(e) for $\vec{S}_{in} = \vec{S}_{L+}$. Each colored curve corresponds to a different membrane. The solid lines and shaded areas designate the average and standard deviation over the four measurement points $\mathbf{r}_{i=1\cdots4}$, respectively. These curves give a more quantitative appreciation of the patterns in the $\Pi_L(\rho, \phi)$-images. It can be seen that they resemble Gaussian distributions and that the higher the degree of alignment, the stronger the curve is peaked [86]. The positions of the peaks designate the azimuthal direction ϕ_{max} of the stretch. In the case where the nanofibers would be aligned precisely along ϕ_{ref}, the patterns in the $\Pi_L(\rho, \phi)$-images would be stretched precisely along $\phi_{max} = \phi_{ref} - \pi/2 = \pi/4$. Yet, this is not the case here ($\phi_{max} \neq \pi/4$), meaning that, for each membrane, the nanofiber alignment direction slightly deviates from the approximate ϕ_{ref}.

Such a radial analysis performed for a single polarization state $\vec{S}_{in}$ of the probing beam does not suffice, by itself, to assess the strength of the anisotropy and the birefringence exhibited by these membranes. It is necessary to evaluate in addition the dependency of ϕ_{max} and of the value of the peak $\langle \Pi_L(\phi = \phi_{max}) \rangle_\rho$ on the orientation of $\vec{S}_{in}$. Thus, we repeated the radial analysis outlined above for different orientations of the probing beam's linear polarization state, $\vec{S}_{in}$, (with a step size of 0.0175 rad), (following the reasoning in, *e.g.*, [62,65,68]): see Figs. 6(a) and (b) and Figs. 6(c) and (d), respectively. The polarimetric response of the membranes for different $\vec{S}_{in}$ was easily obtained in post-processing, without having to repeat the measurements, by using the spatial PM matrix $\mathbf{M}(\rho, \phi)$ recorded at each measurement point $\mathbf{r}_{i=1\cdots4}$. To determine ϕ_{max} and $\langle \Pi_L(\phi_{max}) \rangle_\rho$, we performed numerical fits, whereby a Gaussian model was fitted to the curves

Optics EXPRESS

obtained from the radial analysis for different $\vec{S}_{in}$. Like in Fig. 5(e), each colored curve in the graphs in Fig. 6 corresponds to a different membrane. For better readability of the graphs, we show the results for the non-aligned membrane and the one collected at 2100 rpm separately from the results for the membranes collected at 1000, 1500, and 2000 rpm. The solid lines and shaded areas designate again the average and standard deviation over the four measurement points $\mathbf{r}_{i=1\cdots4}$, respectively.

This set of graphs provide a visualization of the correlation between the anisotropic nature (Figs. 6(a) and (b)) and the birefringent properties (Figs. 6(c) and (d)) of the membranes [87]. It can be seen, for example in the case of the membrane collected at 2100 rpm, that there is no rotational symmetry, *i.e.*, the azimuthal direction along which the patterns in the $\Pi_L(\rho, \phi)$-images are stretched does not significantly depend on the orientation of the probing beam's polarization (see the relatively flat red curve in Fig. 6(a)). This strong anisotropy is correlated with the fact that the linearity of the probing beam's polarization state $\vec{S}_{in}$ is preserved predominantly for two orientations of $\vec{S}_{in}$ (see the two peaks in Fig. 6(b)) that are normal to each other. This is indicative of the birefringence of the membrane, and the two peaks, denoted by $\vec{S}_{\parallel}$ and $\vec{S}_{\perp}$, occur when the orientation of $\vec{S}_{in}$ is parallel and perpendicular to the optic axis (this in turn determines the mean nanofiber alignment direction). Similar observations can be made for the membranes collected at 1500, and 2100 rpm and this confirms what has been suggested by Fig. 5, namely that with increasing degree of alignment, the membranes start to behave like a uniaxially birefringent material.

For comparison, we plotted in Figs. 6(a)-(d) the responses recorded from colloidal suspensions (polystyrene spheres of 175 nm radius diluted in water, so as to have a mean free path length of 1 mm: see [37] for more details), by using the same measurement and data analysis procedure as for the membranes. The perfect rotational symmetry of these suspensions can be seen in the corresponding plots in Figs. 6(a) and (b), as the phi_max rotate when rotating the orientation of $\vec{S}_{in}$ (see the diagonal dashed line). Moreover, the non-birefringence of the suspensions is visible in the plots in Figs. 6(c) and (d), since there is no preferred orientation of $\vec{S}_{in}$ for which the linear polarization is better preserved (see the quasi-flat dashed line). Looking at Figs. 6(a) and (b), it becomes apparent that the non-aligned membrane is equally rotationally symmetric, *i.e.*, isotropic, and does not behave like a birefringent material. The differences, in Fig. 6(a), between the response of the colloidal suspensions and that of the non-aligned membrane are due to noise in the latter [87].

We would like to draw attention to the fact that the plots in Fig. 6 are essential not only because they showcase the correlations between (an)isotropy and (non-)birefringence, but also they can be used to quantify both the mean alignment direction of the nanofibers (see the remark above and Sec. 3.3) and their degree of alignment. Indeed, the curves in Figs. 6(a) and (b) can serve as quantitative indicators of the membranes degree of alignment. The steeper the curve, the more rotationally symmetric and misaligned the nanofibers are. On the contrary, the flatter the curve, the higher the degree of alignment. As a further proof, the similarity between the curves corresponding to the membranes collected at 1000 and 1500 rpm confirm what has been reported in [69], where the analysis of SEM-micrographs as well as Small Angle X-ray scattering (SAXS) have shown that these two membranes have a comparable degree of alignment. Interestingly however, we show here that although the membrane collected at 1000 rpm displays an anisotropic behavior that is similar to that of the membrane collected at 1500 rpm (see the similar trends of the corresponding curves in Fig. 6(b)), the former membrane's birefringent properties are not as pronounced (less clearly visible peaks in Fig. 6(d)).

Our findings can be put in relation to the work of Liao *et al.* [65], where the Authors have empirically derived an analytical indicator for the degree of alignment based on the analysis of the PM matrix, yet without necessarily commenting on its physical significance. This indicator is calculated from the central elements of the PM matrix and is *de facto* related to the degree of

Optics EXPRESS

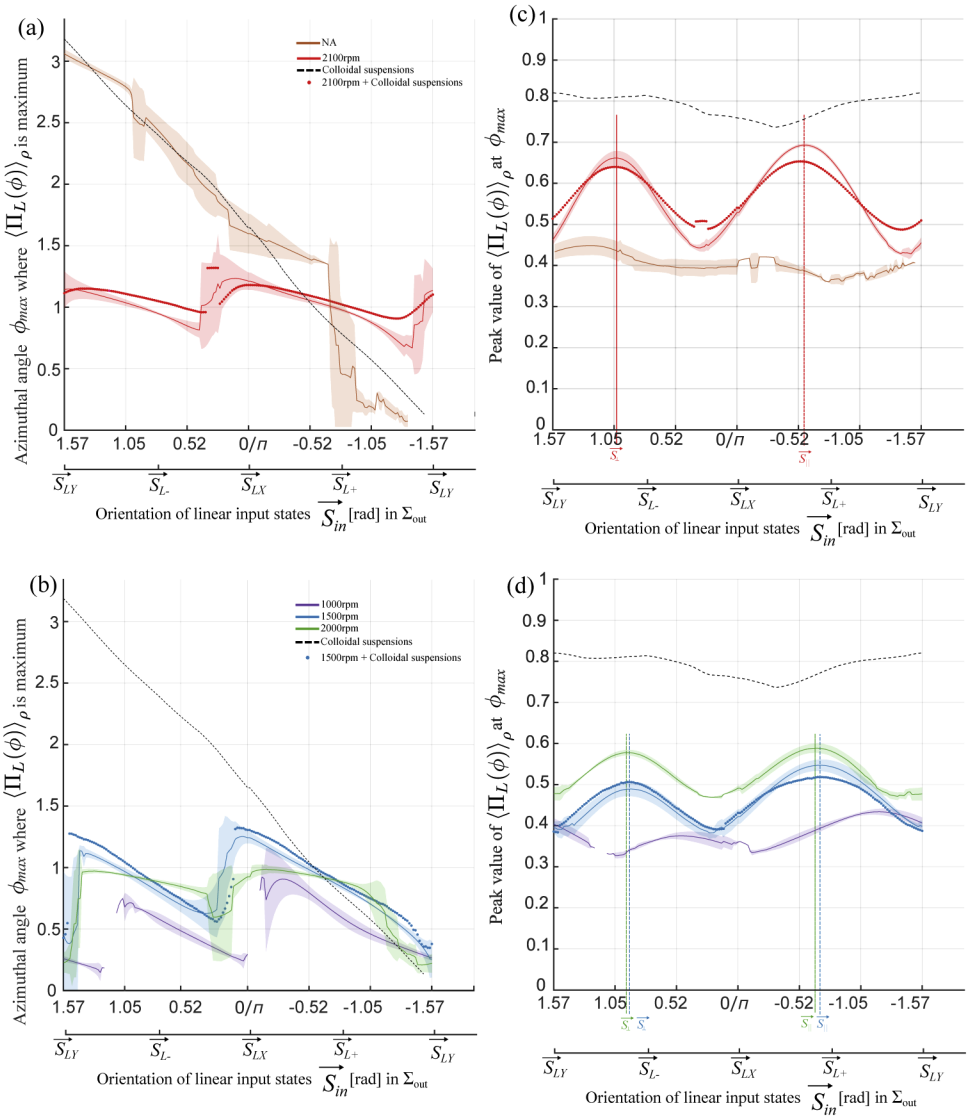

Fig. 6. **(a)** and **(b)**: azimuthal angle ϕ_{max} at which the maximum of $\langle\Pi_L(\phi)\rangle_\rho$ was recorded for different orientations (between $\pi/2$ and $-\pi/2$ in Σ_{out}) of the linear polarization $\vec{S}_{in}$ of the probing beam. **(c)** and **(d)**: peak value of $\langle\Pi_L(\phi)\rangle_\rho$ recorded at ϕ_{max} for different orientations (between 0 and π in Σ_{in}) of the linear polarization $\vec{S}_{in}$ of the probing beam ($\vec{S}_{in}$ is given in different coordinate systems for better representation of the outcomes). ϕ_{max} and $\langle\Pi_L(\phi = \phi_{max})\rangle_\rho$ values are left blank for states $\vec{S}_{in}$ where no Gaussian distribution was identifiable in the radial analysis of the $\Pi_L(\rho, \phi)$-images. The solid lines and shaded areas are the average and standard deviation over points $\mathbf{r}_{i=1\cdots4}$, respectively. For well aligned membranes, the two peaks in **(c)** and **(d)** coincide with orientations of $\vec{S}_{in}$ that are parallel ($\vec{S}_{\parallel}$) and perpendicular ($\vec{S}_{\perp}$) to the optic axis (that is determined by the mean nanofiber alignment direction). To have a reference showcasing quasi-perfect rotational symmetry, we performed the same radial analysis on measurements collected from colloidal suspensions [37] (dashed black lines).

Optics EXPRESS

linear polarization. Our investigation helps, on the one hand, confirm that the degree of linear polarization is a valuable polarimetric indicator for the degree of alignment and on the other hand, better understand the underlying physics.

3.3. Estimating the nanofibers' mean alignment direction

The membranes we probed in this study were such that the nanofibers' approximate alignment direction was visible in the white light images. However, this might not always be the case with biological tissues and it would be interesting, in many applications, to have an estimate for the nanofibers' alignment direction in addition to their degree of alignment (for example in neuroscience, where the human connectome is being reconstructed by unraveling the architecture and connectivity of axon bundles [74,75]).

In principle, the mean alignment direction can be roughly inferred from the PEPs (recall Figs. 4 and 5), *i.e.*, from the direction in which the elliptical patterns in the intensity- and $\Pi(\rho, \phi)$-images are stretched. Note that this direction, corresponding to the average ϕ_{max} of the curves in Figs. 6(a) and (b), unambiguously distinguishes the two peaks observed in the curves in Figs. 6(c) and (d), as - in all aligned membranes - one of the peaks is oriented roughly parallel and the other one roughly perpendicular to ϕ_{max}. As explained previously, if the membrane is anisotropic, the patterns are stretched in the direction perpendicular to the mean nanofiber alignment. The average ϕ_{max} of the red and green curves in Figs. 6(a) and (b), thus indicates the directions perpendicular to the orientation of nano-fibers. A more precise estimation can be obtained from the analysis of the plots in Figs. 6(c) and (d): if the picture of a uniaxially birefringent material holds true, the positions of the two peaks correspond with $\vec{S}_{in} = \vec{S}_{\parallel}$ and $\vec{S}_{in} = \vec{S}_{\perp}$, *i.e.*, orientations of $\vec{S}_{in}$ that are parallel and perpendicular the optic axis determined by the nanofibers mean alignment direction. In Figs. 6(c) and (d), the $\vec{S}_{\parallel}$ and $\vec{S}_{\perp}$ are indicated for all aligned samples. In Figs. 6(a) and (b), a visual comparison confirms the expected angle of these input states in relation to ϕ_{max}.

Here, we wanted to further assess how accurate this picture is and how precisely the mean alignment direction can be calculated. Up to this point, we have only acknowledged the fact the *linearity* of $\vec{S}_{in} = \vec{S}_{\parallel}$ is preserved along the azimuthal direction ϕ_{max}. In order to ascertain that the highly aligned membranes do behave like uniaxially birefringent materials, it is necessary, in addition, to check whether the *orientation* of $\vec{S}_{in} = \vec{S}_{\parallel}$ is preserved along the azimuthal direction ϕ_{max}.

To this end, we started by determining for the aligned membranes and at all four measurement points $\mathbf{r}_{i=1\cdots4}$ the orientation of $\vec{S}_{\parallel}$: see Table 2. For further illustration, we show the same radial analysis as in Fig. 5(e), but for $\vec{S}_{in} = \vec{S}_{\parallel}$. The curves yielded by this analysis are shown in Fig. 7. The solid lines and shaded areas designate the average and standard deviation over the four measurement points $\mathbf{r}_{i=1\cdots4}$, respectively. Although, for visualization purposes, we have represented in Fig. 7 ϕ_{max} averaged over $\mathbf{r}_{i=1\cdots4}$, we give in Table 2 the ϕ_{max}-angles and the standard error obtained separately for each measurement point. Finally, we verified to what extent the orientation of $\vec{S}_{\parallel}$ was preserved along the ϕ_{max}-direction. The mean orientation of the backscattered light's polarization along ϕ_{max} can simply be retrieved from the $\psi(\rho, \phi)$-images in the PEPs (last rows in Fig. 4). The mean orientation values, $\langle \psi(\phi) \rangle_{\rho}$, and standard deviation within $\phi = \phi_{max} \pm$ standard error, we obtained are listed in Table 2, next to the orientations of $\vec{S}_{\parallel}$ and the ϕ_{max}-angles.

A couple of more observations can be made by looking at Fig. 7 and Table 2. First, confirming what has already been observed in Fig. 6, it can be seen for all membranes that the elliptical patterns are indeed in the direction that is perpendicular to the orientation of $\vec{S}_{\parallel}$. Second, the higher the nanofibers' degree of alignment in the membranes, the better the orientation of $\vec{S}_{\parallel}$ is maintained in backscattering along the stretch direction ϕ_{max}. The values in Table 2 further confirm our findings in the Sec. 3.2: in contrary to the membrane collected at 1000 rpm, those collected at 1500, 2000, and 2000 rpm truly behave like uniaxially birefringent materials. As

Optics EXPRESS

Table 2. Quantities retrieved from Figs. 6 and 7 to infer the nanofibers' mean alignment direction at each measurement point $r_{i=1\cdots4}$ on the four aligned membranes (collected at 1000, 1500, 2000, and 2100 rpm). *Third column*: orientation of the probing beam's polarization state $\vec{S}_{in} = \vec{S}_{\parallel}$ (given in Σ_{out}) that corresponds to the position of the second peaks in Figs. 6(c) and (d). *Fourth column*: (i) azimuthal angles ϕ_{max} along which the patterns in the $\Pi_L(\rho,\phi)$-images are stretched when $\vec{S}_{in} = \vec{S}_{\parallel}$. The ϕ_{max} and the standard error values are given by the positions of the peaks and their uncertainty in Fig. 7(a). To verify whether ϕ_{max} is perpendicular to the orientation of $\vec{S}_{\parallel}$ (in Σ_{out}), we also give (ii)$\phi_{max} + \pi/2$. *Fifth column*: Mean orientation $\langle\psi(\phi = \phi_{max} \pm \text{standard error})\rangle_{\rho}$ at ϕ_{max} of backscattered light's polarization in the azimuthal direction $\phi_{max}\pm$ standard error along which the $\Pi_L(\rho,\phi)$-images are stretched. This mean orientation can be retrieved from the $\psi(\rho,\phi)$-images in the PEPs (last rows in Fig. 4) and is given here (i) with the conventions used in the PEPs-representation in Fig. 4 and (ii) the conventions used for the azimuthal directions ϕ. In the case of high degree of alignment (*e.g.*, for the membrane collected at 2100 rpm) the (ii)-values in the three columns coincide with each other and give a reliable estimate for the mean alignment direction of the nanofibers.

PVDFhfp scaffolds (rpm)	Measurement points	Orientation of $\vec{S}_{in} = \vec{S}_{\parallel}$ $[rad]$ in Σ_{out}	Azimuthal angles (i) ϕ_{max} and (ii) $\phi_{max} + \pi/2$ $[rad]$ in Σ_{out}	$\langle\psi(\phi)\rangle_{\rho}$ $[rad]$ at $\phi = \phi_{max}$ (i) in PEPS-convention and (ii) in ϕ-convention
1000	$\mathbf{r}_1$	1.9199	(i) 0.3537±0.0126 (ii) 1.9245±0.0126	(i) −0.7760±0.0523 (ii) 2.3656±0.0523
	$\mathbf{r}_2$	2.0246	(i) 0.4368±0.0165 (ii) 2.0246±0.0165	(i) −0.7249±0.0660 (ii) 2.4167±0.0660
	$\mathbf{r}_3$	1.8151	(i) 0.3233±0.0156 (ii) 1.8151±0.0156	(i) −0.7712±0.0178 (ii) 2.3704±0.0178
	$\mathbf{r}_4$	1.9897	(i) 0.4543±0.0110 (ii) 1.9897±0.0110	(i) −0.7897±0.0293 (ii) 2.3519±0.0293
1500	$\mathbf{r}_1$	2.4435	(i) 0.9023±0.0065 (ii) 2.4731±0.0065	(i) −0.5700±0.0095 (ii) 2.5716±0.0095
	$\mathbf{r}_2$	2.4784	(i) 0.9089±0.0080 (ii) 2.4797±0.0080	(i) −0.6017±0.0094 (ii) 2.5399±0.0094
	$\mathbf{r}_3$	2.4784	(i) 0.9227±0.0080 (ii) 2.4935±0.0080	(i) −0.5665±0.0130 (ii) 2.5721±0.0130
	$\mathbf{r}_4$	2.3910	(i) 0.8281±0.0064 (ii) 2.3989±0.0064	(i) −0.6208±0.0258 (ii) 2.5208±0.0258
2000	$\mathbf{r}_1$	2.4435	(i) 0.9066±0.0076 (ii) 2.4774±0.0076	(i) −0.5644±0.0142 (ii) 2.5772±0.0142
	$\mathbf{r}_2$	2.5307	(i) 0.9027±0.0079 (ii) 2.4735±0.0079	(i) −0.4883±0.0300 (ii) 2.6533±0.0300
	$\mathbf{r}_3$	2.4958	(i) 0.9089±0.0112 (ii) 2.4797±0.0112	(i) −0.4609±0.0216 (ii) 2.6807±0.0216
	$\mathbf{r}_4$	2.4784	(i) 0.9238±0.0122 (ii) 2.4946±0.0122	(i) −0.4828±0.0121 (ii) 2.6588±0.0121
2100	$\mathbf{r}_1$	2.5831	(i) 1.0321±0.0065 (ii) 2.6029±0.0065	(i) −0.4692±0.0134 (ii) 2.6724±0.0134
	$\mathbf{r}_2$	2.5656	(i) 1.0126±0.0052 (ii) 2.5834±0.0052	(i) −0.5393±0.0102 (ii) 2.6023±0.0102
	$\mathbf{r}_3$	2.5831	(i) 1.0583±0.0062 (ii) 2.6291±0.0062	(i) −0.4840±0.0190 (ii) 2.6576±0.0190
	$\mathbf{r}_4$	2.6005	(i) 1.0624±0.0055 (ii) 2.6332±0.0055	(i) −0.4933±0.0365 (ii) 2.6483±0.0365

Optics EXPRESS

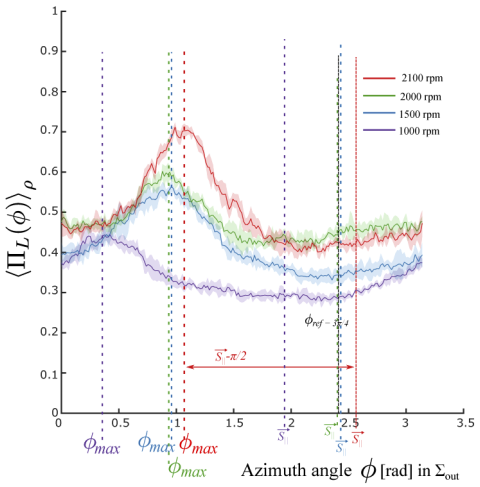

Fig. 7. Outcomes of the radial analysis of the $\Pi_L(\rho, \phi)$-images, analogous to the curves shown in Fig. 5(e). This time however, instead of taking $\vec{S}_{in} = \vec{S}_{L+}$ for all membranes, we chose $\vec{S}_{in} = \vec{S}_{\parallel}$ for each membrane, depending on where the second peak in Fig. 6 appears. Each curve corresponds to a different membrane, where the solid line is $\langle \Pi_L(\phi) \rangle_\rho$ averaged over $\mathbf{r}_{i=1\ldots4}$, and the shaded area is the standard deviation between those points. The positions of the peaks denote the azimuthal direction ϕ_{max} of the stretch. It can be seen, for example for the membrane collected at 2100 rpm, that the orientation of $\vec{S}_{\parallel}$ gives a good estimate of the nanofiber alignment direction, as the patterns in the $\Pi_L(\rho, \phi)$-images appear to be stretched in the direction perpendicular to that orientation.

such, the orientation of $\vec{S}_{\parallel}$ can be used as a reliable estimate for the nanofibers' mean alignment direction. More importantly, the difference between the orientation of $\vec{S}_{\parallel}$ and the mean orientation of the backscattered light's polarization along ϕ_{max} can be used as a measure for the uncertainty of this mean alignment direction. A visual representation of these results is given in Fig. 8.

3.4. *On the relation between the probing beam's polarization state and the probing depth*

The methods that we used to derive information on the microstructural properties of the membranes are actually loosely based on *polarization gating* techniques [24,88,89]. Because our gating technique uses linear polarization, it is confined to the examination of superficial, or *sub-superficial* layers ($<100-200\,\mu$m for the membranes) [90–97]. This was already observable in Fig. 1, where we had shown that the spatial distribution of the backscattered light is very sensitive to the membranes' surface structure. In order to further corroborate this, we repeated the experiments with the membranes collected at 2100 and 1500 rpm, but this time, by placing symmetric colloidal suspensions (identical to the ones used for the reference plots in Fig. 6) underneath them: See the dotted red and blue lines in the graphs in Fig. 6. It can be seen that the outcomes of the radial analysis of the Π_L-patterns remain unchanged, *i.e.*, that the symmetric colloidal suspensions underneath the membranes do not have any significant influence on the $\langle \Pi_L(\phi) \rangle_\rho$-images recorded in backscattering.

However, the fibrous alignment of tissues is often subject to spatial variations, which are not only bound to manifest themselves across the surface of the tissue, but also in depth: as revealed by microscopy studies, tissues are often composed of layers with different anisotropy [31,98,99]. Hence, it would be of great interest, in biomedical applications, to retrieve structural information not only from the surface and sub-surface layers, but also from deeper layers. This is a non-trivial

Optics EXPRESS

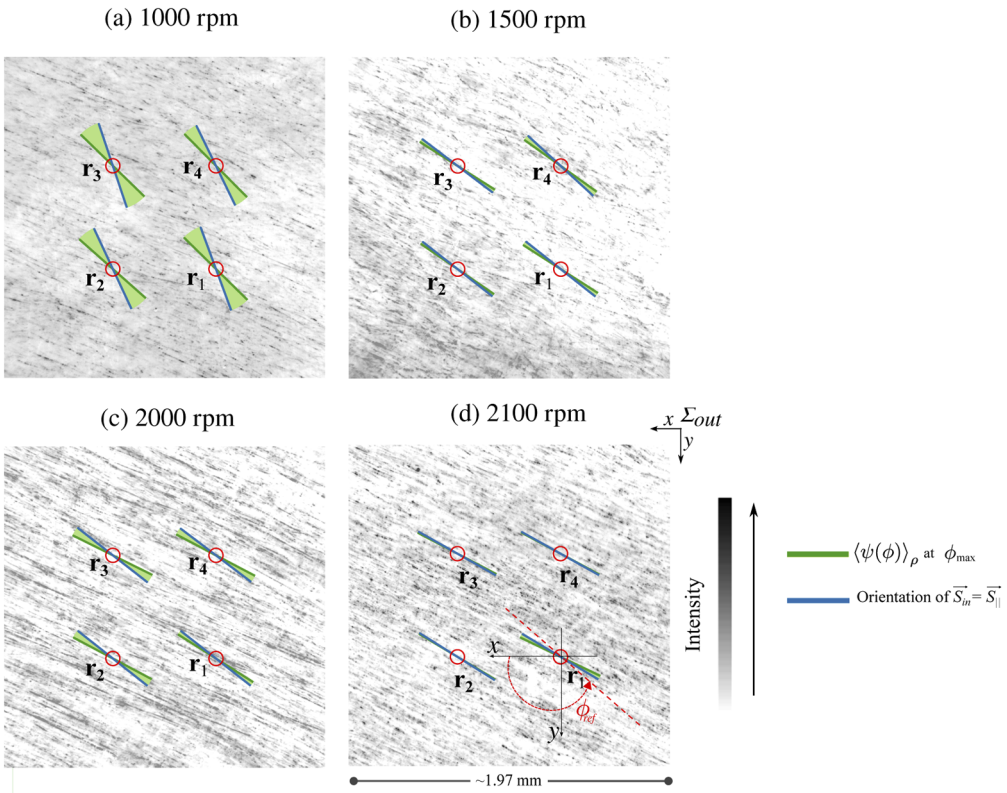

Fig. 8. Estimation of the nanofibers' mean alignment direction for the membranes collected at **(a)** 1000, **(b)** 1500, **(c)** 2000, and **(d)** 2100 rpm at the four different measurement points $\mathbf{r}_{i=1\cdots4}$. This estimation is represented by the blue and green lines, which were drawn based on the azimuthal angles reported in the third and fifth columns in Table 2, respectively. Like in Figs. 3 and 5, these lines are superimposed on the membranes' surface images and the red circles represent the focal spot size and position of the probing beam. The better the alignment of the nanofibers in the membranes, the better the blue and green lines coincide with each other.

task for a number of different reasons. For instance, it has been shown that the shape of the polarimetric patterns observed in backscattering do not necessarily change with the number of scattering events the light has been subject to [45,85,100,101]. Therefore, analyzing only the polarimetric data's spatial variations is insufficient to retrieve depth-dependent information. One would need to also analyze the polarization of the backscattered light as a function of the time the light needed to propagate inside the medium before reaching back the surface [102]. This is done in polarization-sensitive optical coherence tomography (PS-OCT), where the time-resolved measurement of the polarimetric response in turbid media is achieved based on interferometric detection of backscattered photons. The incoherent detection of backscattered light, as used in this study, can potentially be brought closer to PS-OCT via time gating, due to the imminent emergence of the 2D time-resolved cameras [20,103,104]. Alternatively or additionally, one could perform polarization gating using circularly/elliptically polarized illumination instead of a linearly polarized one. An increasing number of polarization imaging techniques [24,93,105,106] exploit circular polarization memory effects [101,107–116] to image greater depths by using finely tuned circular/elliptical polarization. Even though we chose to analyze the degree of linear polarization for sensitive detection of rotational (a)symmetry, the results shown in Fig. 4 reveal

Optics EXPRESS

rich polarimetric information also for other combinations of input/output states, opening the prospect for adapting the analysis to polarization gating.

4. Conclusion

We have presented in this paper an experimental study where fibrous, tissue-like electrospun membranes displaying various degrees of alignment were probed with a polarimeter in the backscattering geometry. These membranes were probed so that the nanofibers were aligned along planes parallel to the imaging plane of the polarimeter. The purpose of this work was twofold: to gain further insight into how the fibrous nature of such materials manifests itself in the measured polarimetric data; and subsequently identify the polarimetric indicators that can help infer the degree of alignment of the fibers in the probed material. The latter point is particularly relevant for tissue diagnostics, as it has been shown that the degree of alignment of the elongated fiber-like macromolecules constitutive of tissue is a valuable indicator for the assessment of tissue pathology. In this paper, we have examined the information contained in the backscattered Stokes vectors (PEPs) separately for different polarization states of the probing beam, by employing symmetry arguments and establishing empirical correlations, in order to determine which polarimetric indicators can help assess the probed membranes' degree of alignment.

Our first observation was that when illuminating the membranes with a "pencil-like" beam, inspecting the spatial arrangement of the backscattered light's degree of linear polarization, $\Pi_L(\rho, \phi)$, can reveal information relevant to the membranes' microstructure. Second, the examination of these $\Pi_L(\rho, \phi)$-images has shown that with increasing degree of alignment, there is a stronger preservation of linear polarization in directions perpendicular to the fiber alignment direction and an increased loss of rotational symmetry, *i.e.*, an increased anisotropic behavior. This is an indication that membranes with highly aligned nanofibers behave like uniaxially birefringent materials, where the optic axis is defined by the fibers' mean alignment direction (when the orientation of the probing beam's polarization is parallel or perpendicular to that alignment direction). In contrast, membranes where the nanofibers are randomly arranged behave like non-birefringent, isotropic materials. Based on these observations, we have outlined a methodology to assess the rotational symmetry of $\Pi_L(\rho, \phi)$-images in order to (i) establish empirical correlations between the anisotropy and the birefringence of the membranes and (ii) showcase, that this can be used as an indicator to deduce the membranes' degree of alignment. Our observations suggest that a measure for the degree of alignment in a fibrous material can be obtained by quantifying how its response deviates from that of a reference material displaying perfect rotational symmetry (*e.g.*, colloidal suspensions diluted in water).

Our investigation was confined to the sub-surface layers of the membranes by the use of linear polarization in illumination and by the analysis of linear states in backscattering. Certainly, the use of elliptically and circularly polarized light for illumination would be equally relevant [117], to probe such materials more in depth. Yet, as we have pointed out, this can be challenging since not only the birefringence of the material but also the scattering from nanofibers has an influence on the ellipticity of the light recorded in backscattering.

Finally, in view of medical applications, future works will involve the probing of fibrous tissue specimen *ex-vivo* to verify whether our methodology can be reproduced and uncover the differences in the degree of alignment in different tissue types.

Funding

Schweizerischer Nationalfonds zur Förderung der Wissenschaftlichen Forschung (173012); Jubiläumsstiftung der Mobiliar.

Optics EXPRESS

Acknowledgments

The authors would like to thank René Nyffenegger and Manes Hornung for their valuable inputs.

Disclosures

The authors declare no conflicts of interest.

Data availability

All data is available on request from the corresponding author.

References

1. N. Ghosh and I. A. Vitkin, "Tissue polarimetry : concepts , challenges , applications , and outlook," J. Biomed. Opt. **16**(11), 110801 (2011).
2. B. Kunnen, C. Macdonald, A. Doronin, S. Jacques, M. Eccles, and I. Meglinski, "Application of circularly polarized light for non-invasive diagnosis of cancerous tissues and turbid tissue-like scattering media," J. Biophotonics **8**(4), 317–323 (2015).
3. A. Pierangelo, A. Benali, M.-R. Antonelli, T. Novikova, P. Validire, B. Gayet, and A. De Martino, "Ex-vivo characterization of human colon cancer by Mueller polarimetric imaging," Opt. Express **19**(2), 1582–1593 (2011).
4. X. Li, J. C. Ranasinghesagara, and G. Yao, "Polarization-sensitive reflectance imaging in skeletal muscle," Opt. Express **16**(13), 9927–9935 (2008).
5. J. M. Bueno and M. C. W. Campbell, "Confocal scanning laser ophthalmoscopy improvement by use of Mueller-matrix polarimetry," Opt. Lett. **27**(10), 830–832 (2002).
6. V. V. Tuchin, "Polarized light interaction with tissues," J. Biomed. Opt. **21**(7), 071114 (2016).
7. M. I. Mishchenko, Y. S. Yatskiv, V. K. Rosenbuch, and G. Videen, "Polarimetric detection, characterization and remote sensing," (Springer, 2011).
8. J. Rička and M. Frenz, "Polarized light: electrodynamic fundamentals," in *Optical-Thermal Response of Laser-Irradiated Tissue*, A. J. Welch and M. J. C. Van Gemert, eds. (Springer, 2011), 2nd ed.
9. T. Courtney, M. S. Sacks, J. Stankus, J. Guan, and W. R. Wagner, "Design and analysis of tissue engineering scaffolds that mimic soft tissue mechanical anisotropy," Biomaterials **27**, 3631–3638 (2006).
10. P. O. Bagnaninchi, Y. Yang, M. Bonesi, G. Maffulli, C. Phelan, I. Meglinski, A. El Haj, and N. Maffulli, "In-depth imaging and quantification of degenerative changes associated with Achilles ruptured tendons by polarization-sensitive optical coherence tomography," Phys. Med. Biol. **55**(13), 3777–3787 (2010).
11. X. Li and G. Yao, "Mueller matrix decomposition of diffuse reflectance imaging in skeletal muscle," Appl. Opt. **48**(14), 2625–2631 (2009).
12. M. F. G. Wood, N. Ghosh, E. H. Moriyama, B. C. Wilson, and I. A. Vitkin, "Proof-of-principle demonstration of a Mueller matrix decomposition method for polarized light tissue characterization in vivo," J. Biomed. Opt. **14**(1), 014029 (2009).
13. S. L. Jacques, J. C. Ramella-Roman, and K. Lee, "Imaging skin pathology with polarized light," J. Biomed. Opt. **7**(3), 329–340 (2002).
14. J. C. Ramella-Roman, K. Lee, S. A. Prahl, and S. L. Jacques, "Design, testing, and clinical studies of a handheld polarized light camera," J. Biomed. Opt. **9**(6), 1305–1310 (2004).
15. Z. Tannous, M. Al-Arashi, S. Shah, and A. N. Yaroslavsky, "Delineating melanoma using multimodal polarized light imaging," Lasers Surg. Med. **41**(1), 10–16 (2009).
16. I. M. Stockford, S. P. Morgan, P. C. Y. Chang, and J. G. Walker, "Analysis of the spatial distribution of polarized light backscattered from layered scattering media," J. Biomed. Opt. **7**(3), 313–320 (2002).
17. D. Kapsokalyvas, N. Bruscino, D. Alfieri, V. de Giorgi, G. Cannarozzo, R. Cicchi, D. Massi, N. Pimpinelli, and F. S. Pavone, "Spectral morphological analysis of skin lesions with a polarization multispectral dermoscope," Opt. Express **21**(4), 4826–4840 (2013).
18. A. Pierangelo, A. Nazac, A. Benali, P. Validire, H. Cohen, T. Novikova, B. H. Ibrahim, S. Manhas, C. Fallet, M.-R. Antonelli, and A.-D. Martino, "Polarimetric imaging of uterine cervix: a case study," Opt. Express **21**(12), 14120–14130 (2013).
19. D. D. Yakovlev, M. E. Schvachkina, M. M. Sherman, A. V. Spivak, A. B. Pravdin, and D. A. Yakovlev, "Quantitative mapping of collagen fiber alignment in thick tissue samples using transmission polarized-light microscopy," J. Biomed. Opt. **21**(7), 071111 (2016).
20. P. Gong, L. Chin, S. Es'haghian, Y. M. Liew, F. M. Wood, D. D. Sampson, and R. A. McLaughlin, "Imaging of skin birefringence for human scar assessment using polarization-sensitive optical coherence tomography aided by vascular masking," J. Biomed. Opt. **19**(12), 126014 (2014).
21. M. A. Wallenburg, M. F. G. Wood, N. Ghosh, and I. A. Vitkin, "Polarimetry-based method to extract geometry-independent metrics of tissue anisotropy," Opt. Lett. **35**(15), 2570–2572 (2010).

Optics EXPRESS

22. M. F. G. Wood, N. Ghosh, M. A. Wallenburg, S.-H. Li, R. D. Weisel, B. C. Wilson, R.-K. Li, and I. A. Vitkin, "Polarization birefringence measurements for characterizing the myocardium, including healthy, infarcted, and stem-cell-regenerated tissues," J. Biomed. Opt. **15**(4), 047009 (2010).
23. T. Novikova, I. Meglinski, J. C. Ramella-roman, and V. V. Tuchin, "Polarized Light for Biomedical Applications," J. Biomed. Opt. **21**(7), 071001 (2016).
24. A. Da Silva, C. Deumié, and I. Vanzetta, "Elliptically polarized light for depth resolved optical imaging," Biomed. Opt. Express **3**(11), 2907–2915 (2012).
25. R. A. Chipman, "Chapter 22: POLARIMETRY," in *Handbook of Optics Volume II: Devices, Measurements, and Properties*, M. Bass, ed. (McGraw Hill, 2009), 2nd ed.
26. N. Ghosh, M. F. Wood, and I. A. Vitkin, "Polarimetry in turbid, birefringent, optically active media: A Monte Carlo study of Mueller matrix decomposition in the backscattering geometry," J. Appl. Phys. **105**(10), 102023 (2009).
27. W. S. Bickel and W. M. Bailey, "Stokes vectors, Mueller matrices, and polarized scattered light," Am. J. Phys. **53**(5), 468–478 (1985).
28. M. Borovkova, L. Trifonyuk, V. Ushenko, O. Dubolazov, O. Vanchulyak, G. Bodnar, Y. Ushenko, O. Olar, O. Ushenko, M. Sakhnovskiy, A. Bykov, and I. Meglinski, "Mueller-matrix-based polarization imaging and quantitative assessment of optically anisotropic polycrystalline networks," PLoS One **14**(5), e0214494 (2019).
29. N. Ghosh, J. Soni, M. F. G. Wood, M. A. Wallenberg, and I. A. Vitkin, "Mueller matrix polarimetry for the characterization of complex random medium like biological tissues," Pramana **75**(6), 1071–1086 (2010).
30. N. Ghosh, M. F. G. Wood, S. Li, R. D. Weisel, B. C. Wilson, R. Li, and I. a. Vitkin, "Mueller matrix decomposition for polarized light assessment of biological tissues," J. Biophotonics **2**(3), 145–156 (2009).
31. S. Alali, Y. Wang, and I. A. Vitkin, "Detecting axial heterogeneity of birefringence in layered turbid media using polarized light imaging," Biomed. Opt. Express **3**(12), 3250–3263 (2012).
32. A. H. Hielscher, J. R. Mourant, and I. J. Bigio, "Influence of particle size and concentration on the diffuse backscattering of polarized light from tissue phantoms and biological cell suspensions," Appl. Opt. **36**(1), 125–135 (1997).
33. J. Dillet, C. Baravian, F. Caton, and A. Parker, "Size determination by use of two-dimensional Mueller matrices backscattered by optically thick random media," Appl. Opt. **45**(19), 4669–4678 (2006).
34. S. Manhas, M. K. Swami, P. Buddhiwant, N. Ghosh, P. K. Gupta, and K. Singh, "Mueller matrix approach for determination of optical rotation in chiral turbid media in backscattering geometry," Opt. Express **14**(1), 190–202 (2006).
35. N. Ghosh, M. F. G. Wood, and I. A. Vitkin, "Mueller matrix decomposition for extraction of individual polarization parameters from complex turbid media exhibiting multiple scattering, optical activity, and linear birefringence," J. Biomed. Opt. **13**(4), 044036 (2008).
36. H. He, N. Zeng, D. L. I. R. Liao, and H. Ma, "Quantitative Mueller Matrix Polarimetry Techniques for Biological Tissues," J. Innovative Opt. Health Sci. **05**(03), 1250017 (2012).
37. M. Hornung, A. Jain, M. Frenz, and H. G. Akarçay, "Interpretation of backscattering polarimetric images recorded from multiply scattering systems: a study on colloidal suspensions," Opt. Express **27**(5), 6210–6239 (2019).
38. R. Ossikovski, M. Anastasiadou, S. Ben Hatit, E. Garcia-Caurel, and A. De Martino, "Depolarizing Mueller matrices: how to decompose them?" Phys. Status Solidi A **205**(4), 720–727 (2008).
39. J. J. Gil, "Review on Mueller matrix algebra for the analysis of polarimetric measurements," J. Appl. Remote Sens **8**(1), 081599 (2014).
40. S.-Y. Lu and R. A. Chipman, "Interpretation of Mueller matrices based on polar decomposition," J. Opt. Soc. Am. A **13**(5), 1106–1113 (1996).
41. Y. Wang, H. He, J. Chang, N. Zeng, S. Liu, M. Li, and H. Ma, "Differentiating characteristic microstructural features of cancerous tissues using Mueller matrix microscope," Micron **79**, 8–15 (2015).
42. N. Ghosh, M. Wood, and A. Vitkin, "Polarized Light Assessment of Complex Turbid Media Such as Biological Tissues Using Mueller Matrix Decomposition," in *Handbook of Photonics for Biomedical Science*, V. V. Tuchin, ed. (CRC, 2010), chap. 9, pp. 253–282.
43. J. Qi and D. S. Elson, "Mueller polarimetric imaging for surgical and diagnostic applications: a review," J. Biophotonics **10**(8), 950–982 (2017).
44. Y. Guo, N. Zeng, H. He, T. Yun, E. Du, R. Liao, Y. He, and H. Ma, "A study on forward scattering Mueller matrix decomposition in anisotropic medium," Opt. Express **21**(15), 18361–18370 (2013).
45. S. Otsuki, "Multiple scattering of polarized light in uniaxial turbid media with arbitrarily oriented linear birefringence," J. Biomed. Opt. **22**(1), 015001 (2017).
46. J. Morio and F. Goudail, "Influence of the order of diattenuator, retarder, and polarizer in polar decomposition of Mueller matrices," Opt. Lett. **29**(19), 2234–2236 (2004).
47. N. Ghosh, M. F. Wood, and I. A. Vitkin, "Influence of the order of the constituent basis matrices on the Mueller matrix decomposition-derived polarization parameters in complex turbid media such as biological tissues," Opt. Commun. **283**(6), 1200–1208 (2010).
48. S. Alali and I. A. Vitkin, "Polarized light imaging in biomedicine: emerging Mueller matrix methodologies for bulk tissue assessment," J. Biomed. Opt. **20**(6), 061104 (2015).
49. R. Ossikovski, "Differential matrix formalism for depolarizing anisotropic media," Opt. Lett. **36**(12), 2330–2332 (2011).

Optics EXPRESS

50. S. Kumar, H. Purwar, R. Ossikovski, I. A. Vitkin, and N. Ghosh, "Comparative study of differential matrix and extended polar decomposition formalisms for polarimetric characterization of complex tissue-like turbid media," J. Biomed. Opt. **17**(10), 105006 (2012).
51. O. Arteaga and A. Canillas, "Analytic inversion of the Mueller - Jones polarization matrices for homogeneous media," Opt. Lett. **35**(4), 559–561 (2010).
52. S.-M. F. Nee, "Decomposition of Jones and Mueller matrices in terms of four basic polarization responses," J. Opt. Soc. Am. A **31**(11), 2518–2528 (2014).
53. H. He, N. Zeng, E. Du, Y. Guo, D. Li, R. Liao, Y. He, and H. Ma, "Two-dimensional and surface backscattering Mueller matrices of anisotropic sphere-cylinder scattering media: a quantitative study of influence from fibrous scatterers," J. Biomed. Opt. **18**(4), 046002 (2013).
54. H. He, N. Zeng, E. Du, Y. Guo, D. Li, R. Liao, and H. Ma, "A possible quantitative Mueller matrix transformation technique for anisotropic scattering media," Photonics Lasers Med. **2**(2), 129–137 (2013).
55. H. He, M. Sun, N. Zeng, E. Du, S. Liu, Y. Guo, J. Wu, Y. He, and H. Ma, "Mapping local orientation of aligned fibrous scatterers for cancerous tissues using backscattering Mueller matrix imaging," J. Biomed. Opt. **19**(10), 106007 (2014).
56. M. Sun, H. He, N. Zeng, E. Du, Y. Guo, S. Liu, J. Wu, Y. He, and H. Ma, "Characterizing the microstructures of biological tissues using Mueller matrix and transformed polarization parameters," Biomed. Opt. Express **5**(12), 4223–4234 (2014).
57. H. He, C. He, J. Chang, D. Lv, J. Wu, C. Duan, Q. Zhou, N. Zeng, Y. He, and H. Ma, "Monitoring microstructural variations of fresh skeletal muscle tissues by Mueller matrix imaging," J. Biophotonics **10**(5), 664–673 (2017).
58. M. Borovkova, M. Peyvasteh, O. Dubolazov, Y. Ushenko, V. Ushenko, A. Bykov, S. Deby, J. Rehbinder, T. Novikova, and I. Meglinski, "Complementary analysis of Mueller-matrix images of optically anisotropic highly scattering biological tissues," J. Eur. Opt. Soc.-Rapid Publ. **14**(1), 20 (2018).
59. T. T. Tower and R. T. Tranquillo, "Alignment maps of tissues: I. Microscopic elliptical polarimetry," Biophys. J. **81**(5), 2954–2963 (2001).
60. T. T. Tower and R. T. Tranquillo, "Alignment maps of tissues: II. Fast harmonic analysis for imaging," Biophys. J. **81**(5), 2964–2971 (2001).
61. I. Ahmad, M. Ahmad, K. Khan, S. Ashraf, S. Ahmad, and M. Ikram, "Ex vivo characterization of normal and adenocarcinoma colon samples by Mueller matrix polarimetry," J. Biomed. Opt. **20**(5), 056012 (2015).
62. X. Wang and L. V. Wang, "Propagation of polarized light in birefringent turbid media: a Monte Carlo study," J. Biomed. Opt. **7**(3), 279 (2002).
63. X. Y. Jiang, N. Zeng, Y. H. He, and H. Ma, "Investigation of linear polarization difference imaging based on rotation of incident and backscattered polarization angles," Prog. Biochem. Biophys. **35**(8), 1233–1240 (2007).
64. T. Yun, N. Zeng, W. Li, D. Li, X. Jiang, and H. Ma, "Monte Carlo simulation of polarized photon scattering in anisotropic media," Opt. Express **17**(19), 16590–16602 (2009).
65. R. Liao, N. Zeng, X. Jiang, D. Li, T. Yun, Y. He, and H. Ma, "Rotating linear polarization imaging technique for anisotropic tissues," J. Biomed. Opt. **15**(3), 036014 (2010).
66. M. K. Swami, H. Patel, M. R. Somyaji, P. K. Kushwaha, and P. K. Gupta, "Size-dependent patterns in depolarization maps from turbid medium and tissue," Appl. Opt. **53**(27), 6133–6139 (2014).
67. S. L. Jacques, S. Roussel, and R. Samatham, "Polarized light imaging specifies the anisotropy of light scattering in the superficial layer of a tissue," J. Biomed. Opt. **21**(7), 071115 (2016).
68. P. Ghassemi, L. T. Moffatt, J. W. Shupp, and J. C. Ramella-Roman, "A new approach for optical assessment of directional anisotropy in turbid media," J. Biophotonics **9**(1-2), 100–108 (2016).
69. A. K. Maurya, L. Weidenbacher, F. Spano, G. Fortunato, R. M. Rossi, M. Frenz, A. Dommann, A. Neels, and A. Sadeghpour, "Structural insights into semicrystalline states of electrospun nanofibers: A multiscale analytical approach," Nanoscale **11**(15), 7176–7187 (2019).
70. K. Susuki, "Myelin: A Specialized Membrane for Cell Communication. Nature Education," https://www.nature.com/scitable/topicpage/myelin-a-specialized-membrane-for-cell-communication-14367205/# (2010).
71. G. H. Bishop and J. M. Smith, "The sizes of nerve fibers supplying cerebral cortex," Exp. Neurol. **9**(6), 483–501 (1964).
72. T. Ushiki, "Collagen fibers, reticular fibers and elastic fibers. A comprehensive understanding from a morphological viewpoint," Arch. Histol. Cytol. **65**(2), 109–126 (2002).
73. D. Liewald, R. Miller, N. Logothetis, H. J. Wagner, and A. Schüz, "Distribution of axon diameters in cortical white matter: an electron-microscopic study on three human brains and a macaque," Biol. Cybern. **108**(5), 541–557 (2014).
74. H. Axer, B. E. Lippitz, and D. G. V. Keyserlingk, "Morphological asymmetry in anterior limb of human internal capsule revealed by confocal laser and polarized light microscopy," Psychiatry Res., Neuroimaging **91**(3), 141–154 (1999).
75. H. Axer, "Microstructural analysis of human white matter architecture using polarized light imaging: views from neuroanatomy," Front. Neuroinform. **5**, 1–12 (2011).
76. E. Compain, S. Poirier, and B. Drevillon, "General and self-consistent method for the calibration of polarization modulators, polarimeters, and Mueller-matrix ellipsometers," Appl. Opt. **38**(16), 3490–3502 (1999).

Optics EXPRESS

77. H. Hu, E. Garcia-Caurel, G. Anna, and F. Goudail, "Maximum likelihood method for calibration of Mueller polarimeters in reflection configuration," Appl. Opt. **52**(25), 6350–6358 (2013).
78. A. Kienle, F. K. Forster, and R. Hibst, "Anisotropy of light propagation in biological tissue," Opt. Lett. **29**(22), 2617 (2004).
79. T. Linder, T. Löfqvist, E. L. G. Wernersson, and P. Gren, "Light scattering in fibrous media with different degrees of in-plane fiber alignment," Opt. Express **22**(14), 16829–16840 (2014).
80. O. Korotkova and D. James, "Definitions of the Degree of Polarization of a Light," Opt. Lett. **32**(9), 1015–1016 (2007).
81. Unfortunate errors seem to have occurred in the typing of the ellipticity and orientation formulas in [37]. We correct for these errors here.
82. H. G. Akarçay, A. Hohmann, A. Kienle, M. Frenz, and J. Rička, "Monte Carlo modeling of polarized light propagation: Stokes vs. Jones. Part I," Appl. Opt. **53**(31), 7576–7585 (2014).
83. H. G. Akarçay, A. Hohmann, A. Kienle, M. Frenz, and J. Rička, "Monte Carlo modeling of polarized light propagation: Stokes vs. Jones. Part II," Appl. Opt. **53**(31), 7586–7602 (2014).
84. E. Du, H. He, N. Zeng, Y. Guo, R. Liao, Y. He, and H. Ma, "Two-dimensional backscattering Mueller matrix of sphere—cylinder birefringence media," J. Biomed. Opt. **17**(12), 126016 (2012).
85. X. Wang and L. V. Wang, "Propagation of polarized light in birefringent turbid media: time-resolved simulations," Opt. Express **9**(5), 254–259 (2001).
86. The different offsets between the curves do not bear any particular significance, as we have determined that they are just a result of the choice of the region of interest across which the radial analysis is performed.
87. Like in Fig. 5 (e) the offsets in Figs. 6 (c) and (d) between the curves do not bear any particular significance, as they are just a result of the choice of the region of interest across which the radial analysis is performed. What is important here is the positions of the peaks.
88. J. M. Schmitt, A. H. Gandjbakhche, and R. F. Bonner, "Use of polarized light to discriminate short-path photons in a multiply scattering medium," Appl. Opt. **31**(30), 6535–6546 (1992).
89. H. Tian, J. P. Zhu, S. W. Tan, J. J. Tian, Y. Y. Zhang, and X. Hou, "Polarization-based range-gated imaging in birefringent medium: Effect of size parameter," Chin. Phys. B **27**(12), 124203 (2018).
90. S. G. Demos, H. Savage, A. S. Heerdt, S. Schantz, and R. R. Alfano, "Time resolved degree of polarization for human breast tissue," Opt. Commun. **124**(5-6), 439–442 (1996).
91. S. G. Demos and R. R. Alfano, "Temporal gating in highly scattering media by the degree of optical polarization," Opt. Lett. **21**(2), 161 (1996).
92. S. G. Demos and R. R. Alfano, "Optical polarization imaging," Appl. Opt. **36**(1), 150–155 (1997).
93. S. Demos, H. Radousky, and R. Alfano, "Deep subsurface imaging in tissues using spectral and polarization filtering," Opt. Express **7**(1), 23–28 (2000).
94. S. L. Jacques, J. R. Roman, and K. Lee, "Imaging superficial tissues with polarized light," Lasers Surg. Med. **26**(2), 119–129 (2000).
95. K. M. Yoo and R. R. Alfano, "Time resolved depolarization of multiple backscattered light from random media," Phys. Lett. A **142**(8-9), 531–536 (1989).
96. M. Dogariu and T. Asakura, "Photon pathlength distribution from polarized backscattering in random media," Opt. Eng. **35**(8), 2234–2240 (1996).
97. A. Dogariu, C. Kutsche, P. Likamwa, G. Boreman, and B. Moudgil, "Time-domain depolarization of waves retroreflected from dense colloidal media," Opt. Lett. **22**(9), 585–587 (1997).
98. T. W. Gilbert, S. Wognum, E. M. Joyce, D. O. Freytes, M. S. Sacks, and S. F. Badylak, "Collagen fiber alignment and biaxial mechanical behavior of porcine urinary bladder derived extracellular matrix," Biomaterials **29**(36), 4775–4782 (2008).
99. K. D. Costa, E. J. Lee, and J. W. Holmes, "Creating alignment and anisotropy in engineered heart tissue: Role of boundary conditions in a model three-dimensional culture system," Tissue Eng. **9**(4), 567–577 (2003).
100. M. J. Raković, G. W. Kattawar, M. B. Mehrubeoğlu, B. D. Cameron, L. V. Wang, S. Rastegar, and G. L. Coté, "Light backscattering polarization patterns from turbid media: theory and experiment," Appl. Opt. **38**(15), 3399–3408 (1999).
101. A. Ambirajan and D. C. Look, "A Backward Monte Carlo Study of the multiple scattering of a polarized laser beam," J. Quant. Spectrosc. Radiat. Transfer **58**(2), 171–192 (1997).
102. I. Berezhnyy and A. Dogariu, "Time-resolved Mueller matrix imaging polarimetry," Opt. Express **12**(19), 4635 (2004).
103. J. F. de Boer and T. E. Milner, "Review of polarization sensitive optical coherence tomography and Stokes vector determination," J. Biomed. Opt. **7**(3), 359–371 (2002).
104. D. Boas, H. Wang, C. Magnain, and B. Fischl, "Polarization-sensitive optical coherence tomography of the human brain connectome," SPIE Newsroom p. 10.1117/2.1201701.006834 (2017).
105. A. J. Gomes, V. Turzhitsky, S. Ruderman, and V. Backman, "Monte Carlo model of the penetration depth for polarization gating spectroscopy: Influence of illumination-collection geometry and sample optical properties," Appl. Opt. **51**(20), 4627–4637 (2012).
106. S. P. Morgan and I. M. Stockford, "Elimination of surface reflections in polarization imaging of superficial tissue," *Annu. Int. Conf. IEEE Eng. Medicine Biol. - Proc.* 3, 2297–2298 (2002).

Optics EXPRESS

107. M. Xu and R. R. Alfano, "Circular polarization memory of light," Phys. Rev. E: Stat., Nonlinear, Soft Matter Phys. **72**(6), 065601 (2005).
108. F. C. MacKintosh, J. X. Zhu, D. J. Pine, and D. A. Weitz, "Polarization memory of multiply scattred light," Phys. Rev. B **40**(13), 9342–9345 (1989).
109. C. M. Macdonald, S. L. Jacques, and I. V. Meglinski, "Circular polarization memory in polydisperse scattering media," Phys. Rev. E: Stat., Nonlinear, Soft Matter Phys. **91**(3), 033204 (2015).
110. A. C. Maggs and V. Rossetto, "Writhing geometry of stiff polymers and scattered light," Eur. Phys. J. B **29**(2), 323–326 (2002).
111. K. G. Phillips, M. Xu, S. K. Gayen, and R. R. Alfano, "Time-resolved ring structure of circularly polarized beams backscattered from forward scattering media," Opt. Express **13**(20), 7954–7969 (2005).
112. S. Rehn, A. Planat-Chrétien, M. Berger, J.-M. Dinten, C. Deumié, and A. da Silva, "Depth probing of diffuse tissues controlled with elliptically polarized light," J. Biomed. Opt. **18**(1), 016007 (2013).
113. S. Sridhar and A. Da Silva, "Enhanced contrast and depth resolution in polarization imaging using elliptically polarized light," J. Biomed. Opt. **21**(7), 071107 (2016).
114. G. Yao and L. V. Wang, "Propagation of polarized light in turbid media: simulated animation sequences," Opt. Express **7**(5), 198–203 (2000).
115. L. F. Rojas-Ochoa, D. Lacoste, R. Lenke, P. Schurtenberger, and F. Scheffold, "Depolarization of backscattered linearly polarized light," J. Opt. Soc. Am. A **21**(9), 1799–1804 (2004).
116. X. Wang, L. V. Wang, C.-W. Sun, and C.-C. Yang, "Polarized light propagation through scattering media: time-resolved Monte Carlo simulations and experiments," J. Biomed. Opt. **8**(4), 608–618 (2003).
117. X. Wang and L. V. Wang, "Propagation of polarized light in birefringent turbid media: time-resolved simulations," Opt. Express **9**(5), 254–259 (2001).